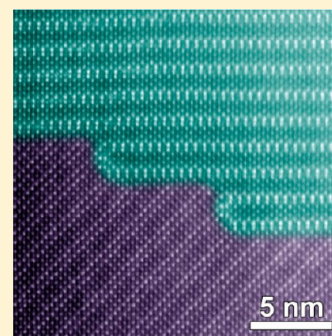


Atomic Structure of Defects in Anion-Deficient Perovskite-Based Ferrites with a Crystallographic Shear Structure

Maria Batuk,^{*,†} Stuart Turner,[†] Artem M. Abakumov,^{†,‡} Dmitry Batuk,[†] Joke Hadermann,[†] and Gustaaf Van Tendeloo[†][†]Electron Microscopy for Materials Research (EMAT), University of Antwerp, Groenenborgerlaan 171, B-2020 Antwerp, Belgium[‡]Department of Chemistry, Moscow State University, 119991 Moscow, Russia

S Supporting Information

ABSTRACT: Crystallographic shear (CS) planes provide a new structure-generation mechanism in the anion-deficient perovskites containing lone-pair cations. $\text{Pb}_2\text{Sr}_2\text{Bi}_2\text{Fe}_6\text{O}_{16}$, a new $n = 6$ representative of the $\text{A}_n\text{B}_n\text{O}_{3n-2}$ homologous series of the perovskite-based ferrites with the CS structure, has been synthesized using the solid-state technique. The structure is built of perovskite blocks with a thickness of four FeO_6 octahedra spaced by double columns of FeO_5 edge-sharing distorted tetragonal pyramids, forming $1/2[110](101)_p$ CS planes (space group $Pnma$, $a = 5.6690(2)$ Å, $b = 3.9108(1)$ Å, $c = 32.643(1)$ Å). $\text{Pb}_2\text{Sr}_2\text{Bi}_2\text{Fe}_6\text{O}_{16}$ features a wealth of microstructural phenomena caused by the flexibility of the CS planes due to the variable ratio and length of the constituting fragments with $\{101\}_p$ and $\{001\}_p$ orientation. This leads to the formation of “waves”, “hairpins”, “T-shaped” defects, and inclusions of the hitherto unknown layered anion-deficient perovskites $\text{Bi}_2(\text{Sr,Pb})\text{Fe}_3\text{O}_{8.5}$ and $\text{Bi}_3(\text{Sr,Pb})\text{Fe}_4\text{O}_{11.5}$. Using a combination of diffraction, imaging, and spectroscopic transmission electron microscopy techniques this complex microstructure was fully characterized, including direct determination of positions, chemical composition, and coordination number of individual atomic species. The complex defect structure makes these perovskites particularly similar to the CS structures in ReO_3 -type oxides. The flexibility of the CS planes appears to be a specific feature of the Sr-based system, related to the geometric match between the SrO perovskite layers and the $\{100\}_p$ segments of the CS planes.



1. INTRODUCTION

Planar defects that change the composition of the parent crystal structure (so-called nonconservative defects) are always fascinating because of their direct relation to compositional flexibility and properties of the materials.^{1–4} Ordering of planar defects leads to new structures or even whole homologous series. In the latter case, changes in chemical composition are caused by stepwise variation of the spacing between the defect planes. Famous examples of compositional changes related to the arrangement of planar defects are provided by crystallographic shear (CS) planes in ReO_3 -type oxides. The three-dimensional cubic framework of the parent ReO_3 structure is built up of corner-sharing ReO_6 octahedra, reminiscent of the perovskite ABO_3 structure with all vacant A positions. The CS mechanism, which reduces the oxygen content, can be represented in the following virtual steps (see Figure 1). The parent framework is cut along a certain $(h0l)$ crystallographic plane (in Figure 1a the orientation of the plane is (103)) and a fraction of the oxygen atoms is removed along the cut. To close the gap, one part of the structure is displaced with respect to another over a vector \mathbf{R} which is a fraction of the basic lattice translation (in Figure 1b $\mathbf{R} = 1/2[10\bar{1}]$).⁵ Constructed in this way, the CS operation reduces the oxygen content, eliminating oxygen vacancies by changing the connectivity scheme of the metal–oxygen (M–O) polyhedra. In ReO_3 -type oxides a CS operation transforms corner-sharing MO_6 octahedra (yellow in

Figure 1b) into edge-sharing octahedra along the CS plane (green in Figure 1b).^{6–8} Any complex CS plane with $(h0l)$ orientation can be considered as a combination of two low-index fragments (001) and (101) with lengths p and q , respectively.⁹ For example, the (103) CS plane in Figure 1 can be represented as $2 \times (001) + 1 \times (101)$ ($p = 2$, $q = 1$). For the displacement vector $\mathbf{R} = 1/2[10\bar{1}]$ along a $(h0l)$ CS plane, the (101) fragment represents the conservative part of the defect (antiphase boundary), since the displacement vector lies within the (101) plane. The (001) fragment is the nonconservative part responsible for the compositional change. A variation of the p and q fractions of the (001) and (101) parts is at the origin of the rich microstructure and compositions of the CS structures. Changing the p/q ratio enables the CS planes to make sideways steps, locally change the orientation and interplanar separation, acquire a wavy shape, and even form U-shape defects, called “hairpins”.^{10,11}

In the ABO_3 perovskites the 12-coordinated cavities of the framework are filled with large A cations, whereas they remain empty in the ReO_3 structure. Oxygen deficiency in perovskites is usually accommodated through oxygen vacancies, which decrease the coordination number of the B cations from 6 (octahedron) to 5 (tetragonal pyramid), 4 (tetrahedron or

Received: November 13, 2013

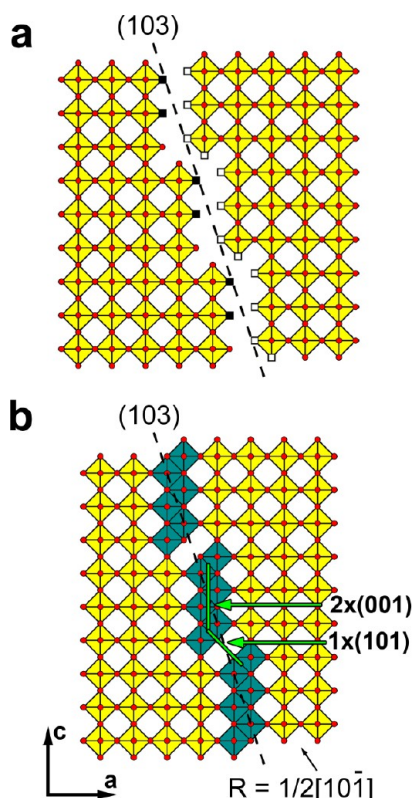


Figure 1. Generation of the $1/2[10\bar{T}](103)$ CS plane in the ReO_3 -type structure: (a) cut of the parent structure along the (103) lattice plane, where the white squares mark the oxygen atoms which appear to be artificially duplicated due to this cut and the black squares mark the oxygen atoms which will be removed due to the shift; (b) application of the $\mathbf{R} = 1/2[10\bar{T}]$ displacement vector, where the (001) and (101) fragments are marked.

planar square), or even 2 (dumbbell).^{12–19} When the A sites in perovskites are at least partially occupied by lone electron pair cations (Pb^{2+} , Bi^{3+}), the oxygen nonstoichiometry can also be accommodated through the CS mechanism, similar to that in ReO_3 -type structures. In perovskites, the CS operation transforms the corner-sharing octahedra into edge-sharing distorted tetragonal pyramids, doing so decreasing the oxygen content with respect to the parent perovskite framework. Examples of the low-index $1/2[110](\bar{1}01)_p$ and $1/2[110](001)_p$ CS planes are shown in Figure 2a,b, respectively (the first part, $1/2[110]$, stands for the displacement vector \mathbf{R} along the CS plane; the second part, $(h0l)_p$, denotes the orientation of the CS plane with respect to the perovskite subcell).^{20–22} CS planes with different $(h0l)_p$ orientations can be realized in perovskite-based structures depending on the ionic radii and electronic configuration of the A and B cations. Compounds with $(\bar{1}01)_p$ CS planes form homologous series by varying the thickness of the perovskite blocks between the neighboring CS planes. The general formula of such a series is $\text{A}_n\text{B}_n\text{O}_{3n-2}$, where $\text{A} = \text{Pb}$, Bi , Ba , Sr , $\text{B} = \text{Fe}$, Sc , Ti , Sn , Mn , Co , and $n = 4–6$ (Figure 2c represents the $n = 6$ member of the series).^{23–33} The number of the homologue n stands for the thickness of the initial perovskite blocks cut by the CS planes, expressed as the number of B–O polyhedra counted in the direction perpendicular to the CS plane (c axis). CS planes with complex $(h0l)_p$ orientations are better described as incommensurately modulated structures, which have been observed in perovskite-based ferrites and manganites.^{21,34–38} Similar to the CS

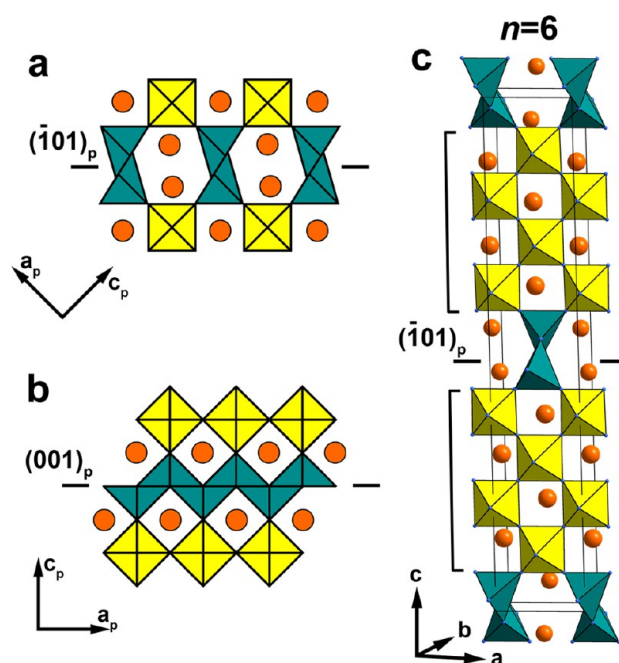


Figure 2. Structures of the low-index CS planes: (a) $1/2[110](\bar{1}01)_p$; (b) $1/2[110](001)_p$. (c) Crystal structure of the $n = 6$ member of the $\text{A}_n\text{B}_n\text{O}_{3n-2}$ homologous series. Perovskite blocks (marked by brackets) are spaced by $1/2[110](\bar{1}01)_p$ CS planes, which transform corner-sharing BO_6 octahedra (yellow) into the edge-sharing BO_5 tetragonal pyramids (blue). Cations A are shown as orange spheres.

structures in binary oxides, the $(h0l)_p$ CS planes in perovskites can be represented through the simple constituting fragments $\{101\}_p$ and $\{001\}_p$. The local variation of the ratio between these fragments can lead to a complex behavior of the CS planes in perovskites.

In this work, we report on the investigation of the new compound $\text{Pb}_2\text{Sr}_2\text{Bi}_2\text{Fe}_6\text{O}_{16}$, which is the $n = 6$ member of the $\text{A}_n\text{B}_n\text{O}_{3n-2}$ series. $\text{Pb}_2\text{Sr}_2\text{Bi}_2\text{Fe}_6\text{O}_{16}$ demonstrates an exceptionally complex microstructure, associated with a peculiar behavior of the CS planes. It was characterized in detail by means of transmission electron microscopy, including the direct determination of atomic positions, chemical composition, and coordination number of the B cations. The study was carried out using aberration-corrected scanning transmission electron microscopy (STEM), providing subangstrom resolution. The visualization of atomic columns of both heavy and light elements is possible with high angle annular dark field (HAADF) and annular bright field (ABF) STEM techniques.^{39,40} The combination of STEM with electron energy-loss spectroscopy (STEM-EELS) or energy-dispersive X-ray (STEM-EDX) spectroscopy allows the acquisition of chemical maps at atomic-column resolution.^{41–46} Mapping of the iron coordination number is possible by STEM-EELS, through mapping of the iron $\text{L}_{2,3}$ EELS fine structure.^{47–49}

2. EXPERIMENTAL SECTION

The $\text{Pb}_2\text{Sr}_2\text{Bi}_2\text{Fe}_6\text{O}_{16}$ samples were synthesized using a high-temperature solid-state reaction of PbO (Sigma-Aldrich, >99.9%), SrCO_3 (Aldrich, >99.9%), Bi_2O_3 (Aldrich, 99.9%), and Fe_2O_3 (Sigma-Aldrich, >99%). The starting materials were mixed in the molar ratio 1:1:0.5:1.5, thoroughly ground, pressed into pellets, and annealed in air at 750 °C for 24 h and at 850 °C for 24 h or at 900 °C for 15 h with intermediate regrinding. Increasing the annealing temperature from 850 to 900 °C alters neither the X-ray powder diffraction pattern nor

the microstructure of the material. A further temperature increase results in a decomposition of the compound, which is associated with the high volatility of lead oxide and the segregation of bismuth strontium ferrite with a perovskite structure.

The bulk chemical composition of the sample was confirmed by energy dispersive X-ray (EDX) spectroscopy analysis performed on a JEOL 5510 scanning electron microscope (SEM) equipped with an INCAx-sight 6587 system (Oxford instruments). The EDX spectra from 90 individual crystallites were measured. The phase analysis of the material was conducted with X-ray powder diffraction (XPD). XPD patterns were recorded on a Huber G670 Guinier diffractometer (Cu $K\alpha_1$ radiation, curved Ge(111) monochromator, transmission mode, image plate).

The samples for transmission electron microscopy (TEM) were made by crushing the powder in ethanol and depositing the suspension on a copper grid covered with a holey carbon film. Selected area electron diffraction (ED) patterns and high angle annular dark field scanning transmission electron microscopy (HAADF-STEM) images were taken on a FEI Tecnai G2 microscope operated at 200 kV. Part of the HAADF-STEM images and annular bright field scanning transmission electron microscopy (ABF-STEM) data were obtained on a FEI Titan 80–300 “cubed” microscope operated at 300 kV and equipped with a probe aberration corrector. Electron energy-loss spectroscopy (STEM-EELS) measurements were performed on the same microscope operated at 120 kV using the same microscope parameters and the procedure elaborated and described in ref 50. EDX-STEM experiments were conducted on an FEI Titan G2 microscope equipped with a Super-X detector and operated at 200 kV. The results were recorded using probes with convergence semiangles in the 21–25 mrad range (with a probe size of about 1 Å). The probe current ranged between 50 and 200 pA. Chemical maps were acquired on a 64 × 64 pixel array using iterative drift correction and with a 25 μ s dwell time.

3. RESULTS

The overall cation composition of the obtained material was determined by SEM-EDX as $\text{Pb}_{1.9(2)}\text{Sr}_{2.0(2)}\text{Bi}_{2.1(2)}\text{Fe}_{6.0(4)}\text{O}_x$, which agrees well with the nominal composition $\text{Pb}_2\text{Sr}_2\text{Bi}_2\text{Fe}_6\text{O}_{16}$. The XPD pattern of $\text{Pb}_2\text{Sr}_2\text{Bi}_2\text{Fe}_6\text{O}_{16}$ can be indexed on an orthorhombic lattice with the unit cell parameters $a = 5.6690(2)$ Å, $b = 3.9108(1)$ Å, and $c = 32.643(1)$ Å (Figure S1 of the Supporting Information). The unit cell parameters are in agreement with those estimated for the $\text{A}_n\text{B}_n\text{O}_{3n-2}$ homologues (Figure 2c) using the formula $a \approx a_p\sqrt{2}$, $b \approx a_p$, $c \approx 9.7$ Å + $(n-2)a_p\sqrt{2}$ ($n = 6$; $a_p \approx 3.9$ Å, the cell parameter of perovskite structure; 9.7 Å is an approximate thickness of the slab between the perovskite blocks).²³ The ED patterns of $\text{Pb}_2\text{Sr}_2\text{Bi}_2\text{Fe}_6\text{O}_{16}$ (Figure S2 of the Supporting Information) confirm the lattice parameters and reveal the $Pnma$ space group, characteristic of low-temperature $\text{A}_n\text{B}_n\text{O}_{3n-2}$ polymorphs with even n .³¹ However, the XPD pattern suffers from a strong asymmetry of the reflections, their hkl -dependent broadening, and their displacements from the ideal positions (a theoretical XPD profile is given in Figure S3 of the Supporting Information). The difference between the theoretical and experimental XPD patterns suggests the presence of numerous extended defects in the structure. To be able to uncover these, transmission electron microscopy was used.

The HAADF-STEM images of $\text{Pb}_2\text{Sr}_2\text{Bi}_2\text{Fe}_6\text{O}_{16}$ are shown in Figure 3 and Figure S4a of the Supporting Information. The brightness of the dots on these images is roughly proportional to the average atomic number Z along the corresponding atomic columns. The brighter pairs of dots in the image are associated with the double Pb/Bi columns ($Z_{\text{Pb}} = 82$, $Z_{\text{Bi}} = 83$). The A positions of the perovskite block are jointly occupied by the Sr/Bi/Pb cations and appear weaker ($Z_{\text{Sr}} = 38$). Dots

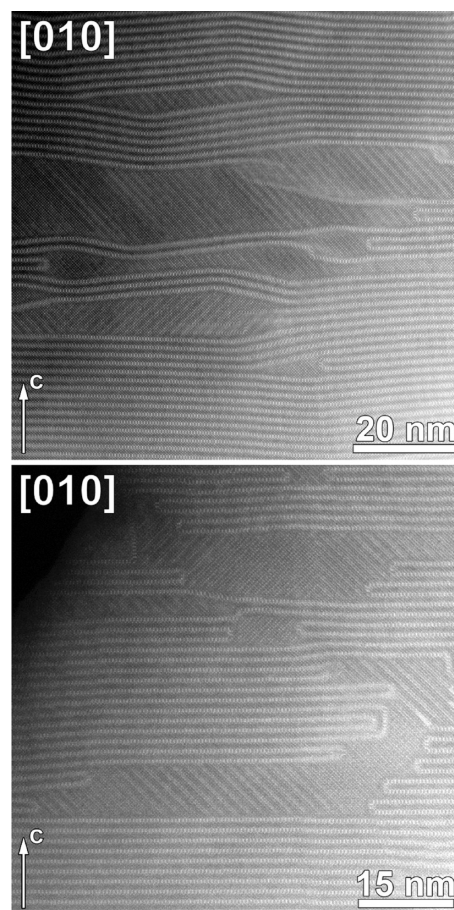


Figure 3. Overview HAADF-STEM images along the [010] direction, indicating the complex defect structure of the $\text{Pb}_2\text{Sr}_2\text{Bi}_2\text{Fe}_6\text{O}_{16}$ crystals.

corresponding to the Fe–O columns are pale, since $Z_{\text{Fe}} = 26$ and $Z_{\text{O}} = 8$. The atomic arrangement conforms to the $\text{A}_6\text{B}_6\text{O}_{16}$ structure with $1/2[110]_p(101)_p$ CS planes^{23,31} (see Figure 2c).⁷⁸ The pairs of Pb/Bi columns are situated inside the six-sided tunnels formed by the FeO_6 octahedra sharing corners with the double columns of edge-sharing FeO_5 distorted tetragonal pyramids (Figure S4b of the Supporting Information). These double columns can occur in two distinct mirror-related configurations, arbitrarily called “left” (L) and “right” (R). The ordering of these configurations in alternating layers is at the origin of polymorphism in the $\text{A}_n\text{B}_n\text{O}_{3n-2}$ homologues.^{26,27,33} In $\text{Pb}_2\text{Sr}_2\text{Bi}_2\text{Fe}_6\text{O}_{16}$, violation of the perfect L–R–L–R sequence of layers was occasionally observed (Figure S4a of the Supporting Information). However, this type of defect is not relevant to the study presented in the current paper.

The most exciting and peculiar defects are associated with deviations of the orientation of the CS planes from $(101)_p$ and segregation of an anion-deficient perovskite-based phase between several adjacent CS planes (Figure 3). These defects will be further analyzed in detail.

In the HAADF-STEM image in Figure 4 the CS planes appear as wavy rows of double Pb/Bi columns. Although the orientation of the CS planes significantly deviates from $(101)_p$, short $(101)_p$ segments can still be identified (they are marked by white straight lines in Figure 4). The $(101)_p$ segments within one CS plane are separated by $(001)_p$ or $(100)_p$ fragments that introduce steps. A high-magnification HAADF-STEM image of

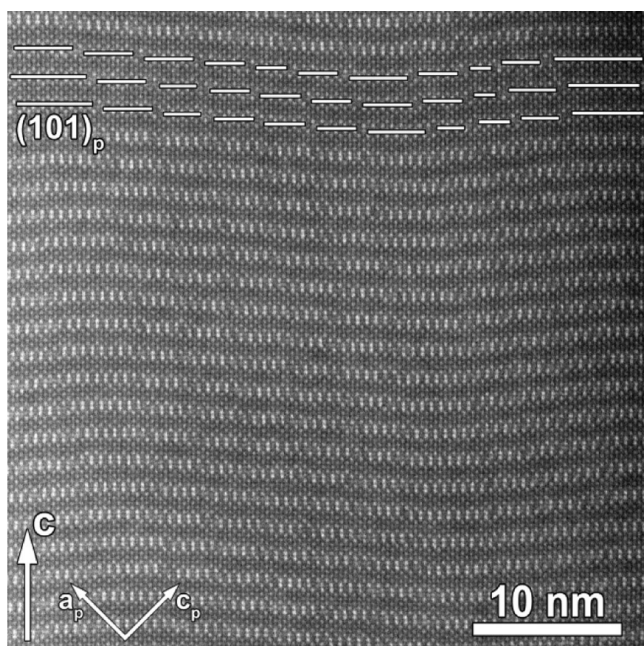


Figure 4. [010] HAADF-STEM image of a crystallite with a fluctuating orientation of the CS planes. The $(101)_p$ fragments of the CS planes are marked as white lines on top of the image.

such a step is shown in Figure 5a. The cation arrangement within this structural fragment can be inferred directly from the image (Figure 5b). It strongly resembles the $(001)_p$ CS plane segments found in the $(\text{Pb,Bi})_{1-x}\text{Fe}_{1+x}\text{O}_{3-y}$ family of anion-deficient perovskites modulated by $\sim(509)_p$ CS planes.³⁵ On the basis of the structure of these compounds the coordination environment of the cations can be provisionally completed with the O atoms (Figure 5d). The $(001)_p$ segments of the CS planes are built of quadruple square-pyramidal chains. Similar to the double-pyramidal chains of the $(101)_p$ CS planes, the pyramids in the quadruple chains are connected by sharing basal edges. The simulated HAADF-STEM image of the constructed model, calculated using the QSTEM 2.0 software,⁵¹ is in good agreement with the experimental image (Figure 5c).

As can be seen in Figure 4, the length q of the $(101)_p$ segments varies significantly, being on average between three and nine repeat periods of the perovskite unit cell. The $(001)_p$ or $(100)_p$ fragments introduce the steps. The length p of such a fragment is always one perovskite repeat period (along $[100]_p$ for the $(001)_p$ fragment or along $[001]_p$ for the $(100)_p$ fragment). Thus, the orientation of the CS planes depends on the length of the $(101)_p$ segments and the type of steps separating them (either $(001)_p$ or $(100)_p$). It is noteworthy that the CS planes change their orientation cooperatively, because the thickness of the perovskite blocks between the CS planes is restricted by the Fe oxidation state and oxygen content. The fluctuating orientation of the CS planes results in a crosslike diffuse intensity on the $[010]$ ED pattern (see Figure S5 of the Supporting Information). A detailed description of the ED patterns performed with the formalism of superspace crystallography⁵² is given in the Supporting Information. As a result of the ED pattern analysis one can estimate the chemical composition of the structure with a fluctuating orientation of the CS planes. It is $(\text{Pb,Sr})_{4.092}\text{Bi}_{1.842}\text{Fe}_{6.066}\text{O}_{15.954}$, with an average separation between the CS planes of 4.3 FeO_6 octahedra along the a_p axis (see the Supporting Information

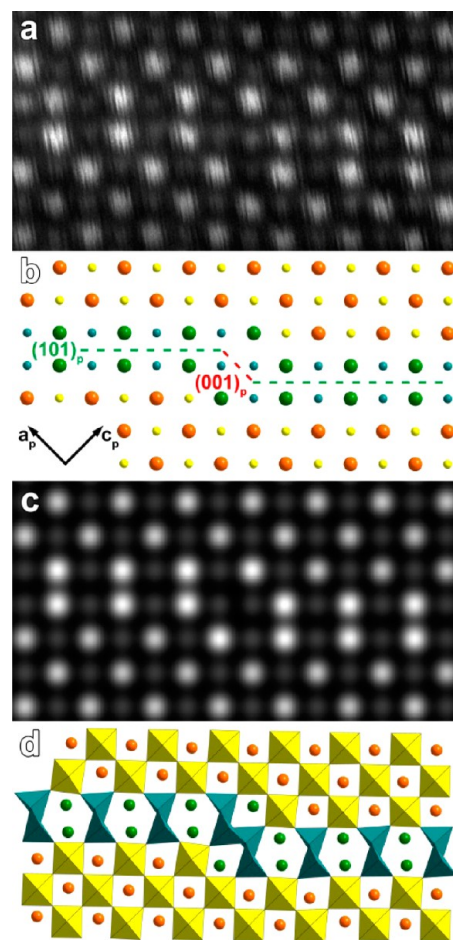


Figure 5. (a) Enlarged HAADF-STEM image of a sideways step. (b) Arrangement of the cation columns. Green spheres correspond to Pb columns, orange to Sr, and small blue and yellow spheres to Fe. The interface is represented as a combination of the fragments $(101)_p$ (green) and $(001)_p$ (red) CS planes. (c) Calculated HAADF-STEM image. (d) Structure model with the FeO_5 (blue) and FeO_6 (yellow) polyhedra.

for details). The average number of FeO_6 octahedra is close to the number found in the $n = 6$ structure, where they are 4. The chemical composition is also not very far from the nominal $\text{Pb}_2\text{Sr}_2\text{Bi}_2\text{Fe}_6\text{O}_{16}$ composition but demonstrates a clear Bi depletion. Below we will show that the remaining Bi is situated in the inclusions of the perovskite phase between the CS planes.

The CS planes are often terminated by “hairpins”, which appear as U-turns in the HAADF-STEM images (Figure 3). A high-magnification HAADF-STEM image of such a defect is shown in Figure 6. This fragment can be also described as a combination of the following low-index fragments:

$$\begin{aligned} &\infty \times (101)_p + 1/2 \times (001)_p + 2 \times (\bar{1}01)_p \\ &+ 3/2 \times (100)_p + \infty \times (101)_p \end{aligned}$$

where the length of the fragments is indicated as the number of perovskite repeat periods along the $[100]_p$, $[101]_p$, and $[001]_p$ directions for the $(001)_p$, $(\bar{1}01)_p$, and $(100)_p$ planes, respectively. In addition to the “hairpin”-type defects, angular defects (“T-shaped” fragments) are formed (Figure 7). Instead of terminating two neighboring CS planes, these defects form a

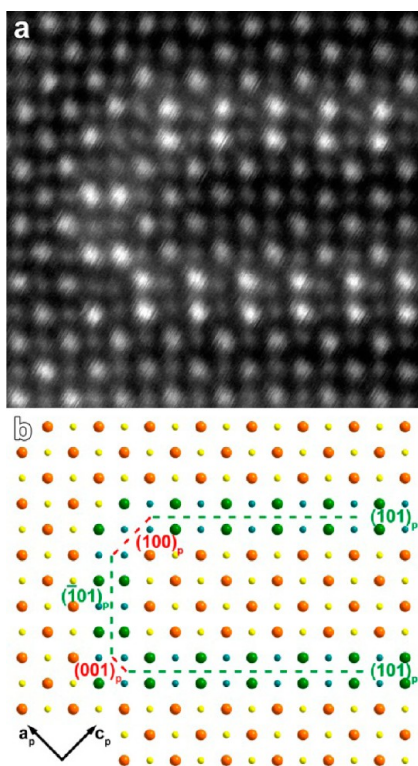


Figure 6. (a) Enlarged HAADF-STEM image of a “hairpin”-like defect. (b) Model showing the distribution of the cation columns. Green spheres correspond to Pb columns, orange to Sr, and small blue and yellow spheres to Fe.

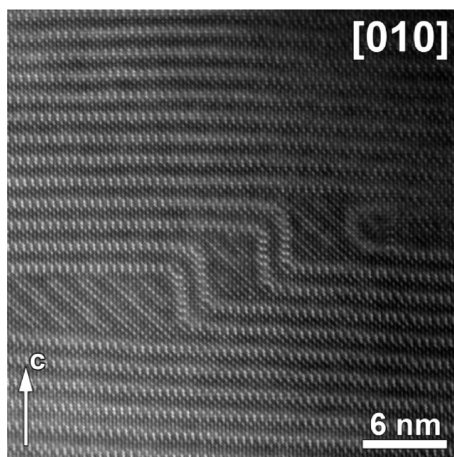


Figure 7. HAADF-STEM image of $\text{Pb}_2\text{Sr}_2\text{Bi}_2\text{Fe}_6\text{O}_{16}$ showing the “T-shaped” defects.

large step from one $(101)_p$ fragment to another. These defects can be described as

$$\infty \times (101)_p + 1 \times (001)_p + k \times (\bar{1}01)_p + 1 \times (001)_p + \infty \times (101)_p$$

Figure 8 shows atomic resolution STEM-EDX maps of an area that includes CS planes and a “hairpin”-like defect. According to the maps, the A positions on the CS planes and “hairpins” are mainly occupied by Pb atoms. Sr is detected in the A positions of the perovskite blocks, and Bi is equally distributed among all A sites.

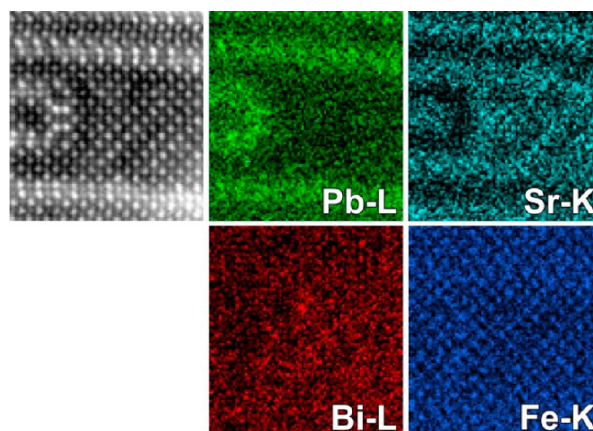


Figure 8. HAADF-STEM images from the area with CS planes and “hairpin”-like defects together with STEM-EDX chemical maps for Pb, Sr, Bi, and Fe from the same area.

The “hairpin” and “T-shaped” defects are typically accompanied by perovskite blocks of a significantly increased thickness. The thickness of such perovskite inclusions can vary over a wide range, up to more than 50 perovskite unit cells. According to the HAADF-STEM images (Figure 3), the structure of such inclusions is characterized by a layered A cation ordering. The HAADF-STEM image of an inclusion is given in Figure 9. The bright dots are attributed to the Pb/Bi/Sr columns, forming a square pattern with a spacing of ~ 4.0 Å, matching the A positions of the perovskite structure. Layered A cation ordering occurs along the c_p direction: two layers of the brighter dots (designated as “A2” columns) alternate with either one or two layers of less bright dots (designated as “A1” columns). The brightness difference is more pronounced on the enlarged images and the corresponding intensity profiles. Some areas possess perfectly ordered structures (for example, A2–A1–A1–A2; see Figure S6 of the Supporting Information), while others form intergrowths, such as in Figure 9, where A2–A1–A1–A2 and A2–A1–A2 fragments are present simultaneously. Because of the layered ordering, the periodicity along the c_p direction increases: $c \approx 3a_p$ for the A2–A1–A2 ordering, and $c \approx 4a_p$ for A2–A1–A1–A2 ordering.

Complementary HAADF-STEM and ABF-STEM images from an inclusion are shown in Figure 10a,b. In the ABF-STEM image, the darker dots are associated with the projections of the A2 columns and the lighter dots correspond to the projected A1 columns. Dots of the Fe–O columns and pure oxygen columns are weak yet visible. Between the neighboring A1 layers as well as between A1 and A2 layers, the O columns are clearly seen at the positions characteristic for the perovskite structure (the corresponding projected octahedra are outlined with blue lines in Figure 10c). One can notice that the oxygen columns of the FeO_2 layer between the A1 and A2 layers are shifted toward the A2 layers. The dots corresponding to the FeO_x layers sandwiched between adjacent A2 layers appear considerably blurred, indicating an oxygen deficiency in these layers. Some oxygen columns in the layers are completely absent; they are marked by squares in Figure 10c. The oxygen deficiency leads to a lack of coordination environment for the A2 cations, which is compensated by a shift of the oxygen atoms in the FeO_2 layer between A1–A2 layers toward the A2 layer.

Elemental STEM-EDX maps of the inclusion with an A2–A1–A1–A2 ordering are shown in Figure 11. The EDX maps

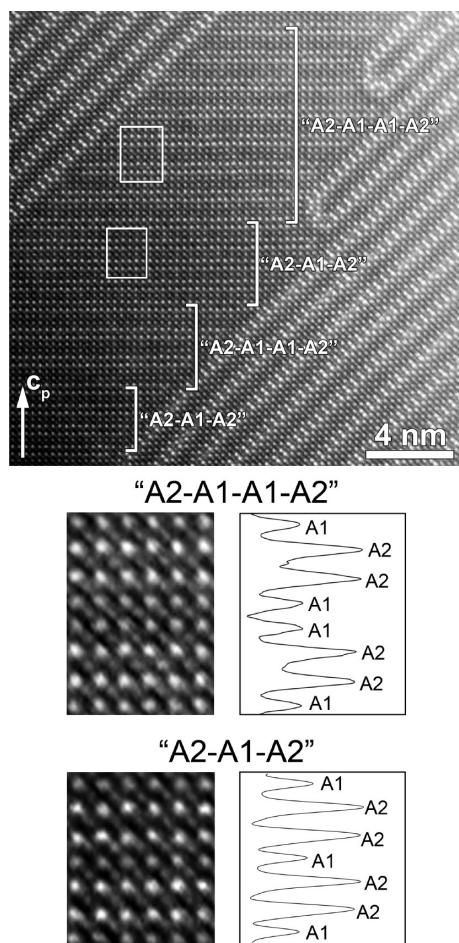


Figure 9. [010] HAADF-STEM image from the area with a perovskite-structure-type inclusion. Parts with “A2–A1–A1–A2” and “A2–A1–A2” ordering are indicated with brackets. For both types of ordering the areas are outlined. The enlarged fragments together with the corresponding intensity profiles are shown at the bottom of the image. Less bright A layers are designated as “A1” and brighter as “A2”.

demonstrate that the A1 columns are occupied mainly by Sr with some amount of Bi and the A2 columns are occupied mainly by bismuth with some amount of Sr. Although the signal of Pb on the EDX spectra is rather low, a small Pb signal is detected in both A2 and A1 positions (the compositions of the A2 and A1 positions will therefore be designated as $\text{Bi}_{1-x}(\text{Sr,Pb})_x$ and $\text{Sr}_{1-y}(\text{Bi,Pb})_y$, respectively). On the basis of both the STEM-EDX results and the analysis of the intensity distribution on the HAADF-STEM images (see Figure S7 in the Supporting Information), one can speculate that Bi and Sr are intermixed in the A1 and A2 layers with the prevalence of Sr in the A1 layers and Bi in the A2 layers.

The EELS spectra shown in Figure 12a indicate that the fine structure of the spectrum measured from the FeO_x layers between two A2 layers (red curve) is significantly different from that of the FeO_2 layer between the A1 and A2 layers (blue curve) (for details see the Supporting Information and ref 50). The position of the L_3 peak on both spectra corroborates the Fe oxidation state +3.^{49,53–55} The blue EELS spectrum is characteristic for Fe in octahedral coordination environment,^{49,50} whereas the red EELS spectrum corresponds to a lower oxygen coordination, most likely being a 5-fold rather than a 4-fold coordination of iron.⁵⁰ The maps in Figure 12b

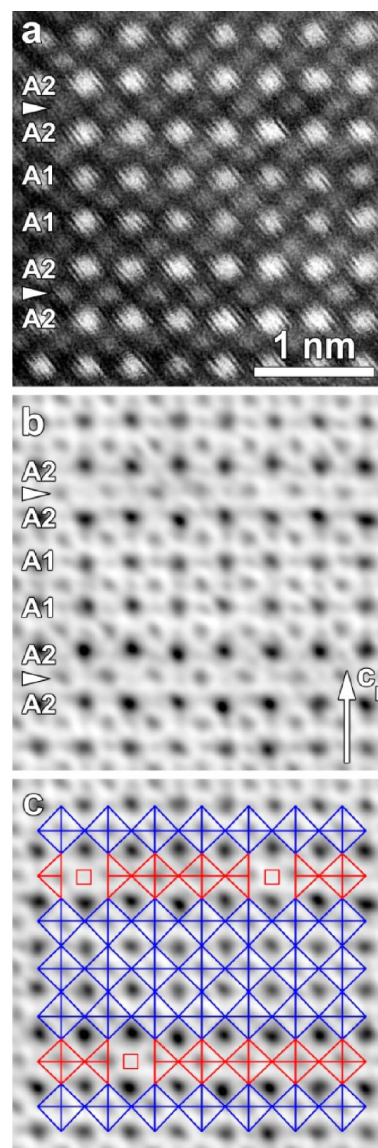


Figure 10. Complementary HAADF-STEM (a) and ABF-STEM (b) images. (c) Image representing the ABF-STEM image (b) with outlined polyhedra. Projected octahedra in the perovskite blocks are shown with blue lines; polyhedra in oxygen-deficient layers are shown with red lines. Red squares indicate oxygen vacancies.

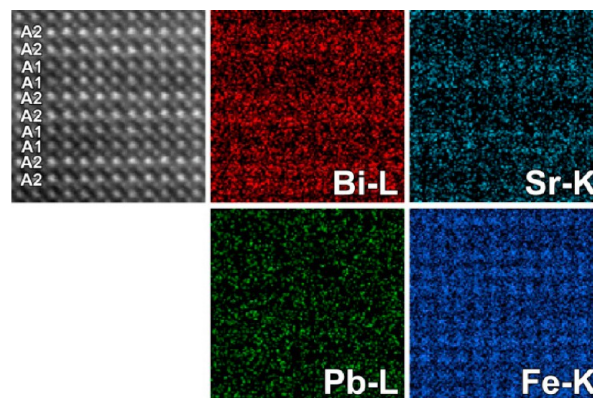


Figure 11. HAADF-STEM image from the area with an A2–A1–A1–A2 layer alternation and STEM-EDX chemical maps for Bi, Sr, Fe, and Pb from the same area.

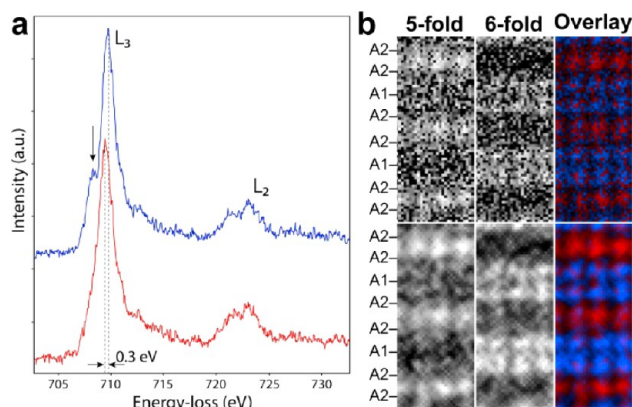


Figure 12. (a) EELS spectra from the 6-fold coordinated Fe sites (blue) and 5-fold coordinated Fe sites (red). (b) Column by column coordination mapping. Fe in octahedral coordination is blue; Fe in tetragonal-pyramidal coordination is red (top, experimental EELS maps; bottom, maps after low-pass filtering).

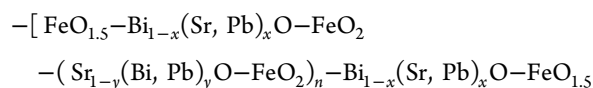
reveal that the B positions between the A1 and A2 layers and between two A1 layers are occupied by iron in a 6-fold coordination, corresponding to the FeO_2 composition, whereas positions between two A2 layers are taken by iron in a 5-fold coordination, corresponding to the $\text{FeO}_{1.5}$ composition. This confirms the conclusion on the layered ordering of oxygen vacancies made from the ABF-STEM images.

4. DISCUSSION

The $\text{Pb}_2\text{Sr}_2\text{Bi}_2\text{Fe}_6\text{O}_{16}$ material demonstrates an exceptionally rich and complex microstructure. The perovskite structure is fragmented by crystallographic shear planes, which on average adopt the $(101)_p$ orientation, resulting in a $Pnma$ orthorhombic structure reminiscent of that of the $n = 6$ member of the $\text{A}_n\text{B}_n\text{O}_{3n-2}$ homologous series.^{23,31} However, numerous defects are present, which are caused by the significant fluctuations in the orientation of the CS planes: i.e., abrupt turns due to the “T-shaped” defects or even termination of the CS planes due to the “hairpin”-type defects. Although, at first glance, these defects seem to be very different, they are all based on the insertion of $(100)_p$ or $(001)_p$ segments of the CS planes between $(101)_p$ segments. The microstructural behavior of the Sr-based system significantly differs from that of the Ba-based system. In the Ba-based $\text{A}_n\text{B}_n\text{O}_{3n-2}$ compounds with the $(101)_p$ CS planes $\text{PbBaFe}_2\text{O}_5$ ($n = 4$), $\text{Pb}_2\text{Ba}_2\text{BiFe}_5\text{O}_{13}$ ($n = 5$), and $\text{Pb}_{1.5}\text{Ba}_{2.5}\text{Bi}_2\text{Fe}_6\text{O}_{16}$ ($n = 6$), defects are associated with a violation of the ordered sequence of the L and R tunnels and an occasional variation of the thickness of the perovskite blocks (stacking faults).^{26,31} Fluctuation of the CS planes orientation and, moreover, formation of the “hairpin” and “T-shaped” defects were not observed in the Ba-based compounds. One can speculate that the large Ba^{2+} cations prevent the formation of $(100)_p$ or $(001)_p$ segments, which are responsible for the variation of the CS plane orientation. These segments are geometrically quite rigid, as they are composed of sheets of edge-sharing FeO_5 pyramids (see Figure 5d). Layers with a similar geometry are formed in the $\text{Sr}_4\text{Fe}_6\text{O}_{12+2\alpha}$ compounds,^{56–58} where they alternate with the $-\text{SrO}-\text{FeO}_2-\text{SrO}-$ perovskite blocks. This demonstrates the geometric match of the $(100)_p$ and $(001)_p$ segments with the in-plane dimensions of the SrO perovskite layer and explains the tendency of the Sr-based system to adopt such fragments. For the larger Ba^{2+} cations ($r(\text{Ba}^{2+}) = 1.61 \text{ \AA}$, $r(\text{Sr}^{2+}) = 1.44 \text{ \AA}$, CN

= 12), similar $\text{Ba}_4\text{B}_6\text{O}_{12+2\alpha}$ structures cannot be obtained with the Fe^{3+} cation ($r = 0.645 \text{ \AA}$, CN = 6, high-spin state) but can be stabilized with larger B cations: e.g., In^{3+} ($r = 0.80 \text{ \AA}$, CN = 6) and Mg^{2+} ($r = 0.72 \text{ \AA}$, CN = 6).^{59,60}

Termination of the CS planes or abrupt variation of their orientation results in extended anion-deficient inclusions between the CS planes. These inclusions have a perovskite-based structure with layered ordering of the A cations coupled with a layered ordering of the oxygen vacancies. Two bismuth-rich $\text{Bi}_{1-x}(\text{Sr,Pb})_x$ (A2) layers alternate either with one or two strontium-rich $\text{Sr}_{1-y}(\text{Bi,Pb})_y$ (A1) layers. According to STEM-EELS, the $\text{FeO}_{1.5}$ layer between two adjacent $\text{Bi}_{1-x}(\text{Sr,Pb})_x$ layers consists of FeO_5 tetragonal pyramids. In the ABF-STEM images the oxygen vacancies in such $\text{FeO}_{1.5}$ layers appear to be disordered (an ABF-STEM image from a large area is shown in Figure S9 of the Supporting Information). The structure can be represented as a stack of the following layers along the c_p axis:



where $n = 1, 2$; and the resulting composition is $\text{Bi}_2(\text{Sr,Pb})\text{Fe}_3\text{O}_{8.5}$ for the A2–A1–A2 ordering and $\text{Bi}_3(\text{Sr,Pb})\text{Fe}_4\text{O}_{11.5}$ for the A2–A1–A1–A2 ordering. The crystal structure of these tentative phases can be modeled using the TEM data. Taking into account the A site ordering, the random distribution of the anion vacancies in the $\text{FeO}_{1.5}$ layers, and the fact that the inclusions seamlessly coalesce with the perovskite blocks of the CS ($\text{Pb}_2\text{Sr}_2\text{Bi}_2\text{Fe}_6\text{O}_{16}$) structure, one can deduce that the unit cell parameters of $\text{Bi}_2(\text{Sr,Pb})\text{Fe}_3\text{O}_{8.5}$ and $\text{Bi}_3(\text{Sr,Pb})\text{Fe}_4\text{O}_{11.5}$ are related to those of the perovskite sublattice as $a \approx a_p$, $b \approx b_p$, $c \approx 3c_p$ and $a \approx a_p$, $b \approx b_p$, $c \approx 4c_p$, respectively. The parameters of the perovskite subcell of the $\text{A}_6\text{B}_6\text{O}_{16}$ CS structure are $a_p = c_p \approx 3.929 \text{ \AA}$, $b_p \approx 3.911 \text{ \AA}$, and monoclinic angle $\beta = 92.4^\circ$ (for details see the Supporting Information). Owing to the coherent intergrowth of the inclusions and the CS structure, the parameters of the perovskite sublattices of these structures must be metrically close. However, careful analysis of the HAADF-STEM images reveals that the monoclinic angle β of $\text{Bi}_2(\text{Sr,Pb})\text{Fe}_3\text{O}_{8.5}$ and $\text{Bi}_3(\text{Sr,Pb})\text{Fe}_4\text{O}_{11.5}$ is rather close to 90° (see Figure S10 of the Supporting Information). Therefore, for simplicity, an orthorhombic $Pmmm$ symmetry has been assumed. To construct the structural model of $\text{Bi}_3(\text{Sr,Pb})\text{Fe}_4\text{O}_{11.5}$ with the A2–A1–A1–A2 ordering, the x and y coordinates of the atoms in all layers were fixed to be either 0 or 1/2. The z coordinates were estimated from the ABF-STEM images. It was done by measuring the intensity profiles of the atomic rows along the z direction and fitting them with a set of Gaussian peaks in the Fityk software.⁶¹ Positions of the peaks were used to determine relative atomic coordinates (Table S1 of the Supporting Information). The resulting structural model is shown in Figure 13. Two limiting cases are illustrated for the oxygen-deficient $\text{FeO}_{1.5}$ layers. In the first case the FeO_5 pyramids are arranged in such a way that vacant oxygen positions form chains along the b_p direction. In the ABF-STEM images these chains are seen as missing oxygen columns. In the second case the vacant and occupied oxygen positions form a chess-board arrangement within the layer. Viewed along the b_p axis, this arrangement produces diffuse spots on the ABF-STEM images. On the basis of the TEM data, one can assume that in the real structure these limiting configurations are combined. The structure of $\text{Bi}_2(\text{Sr,Pb})\text{Fe}_3\text{O}_{8.5}$ is similar to that

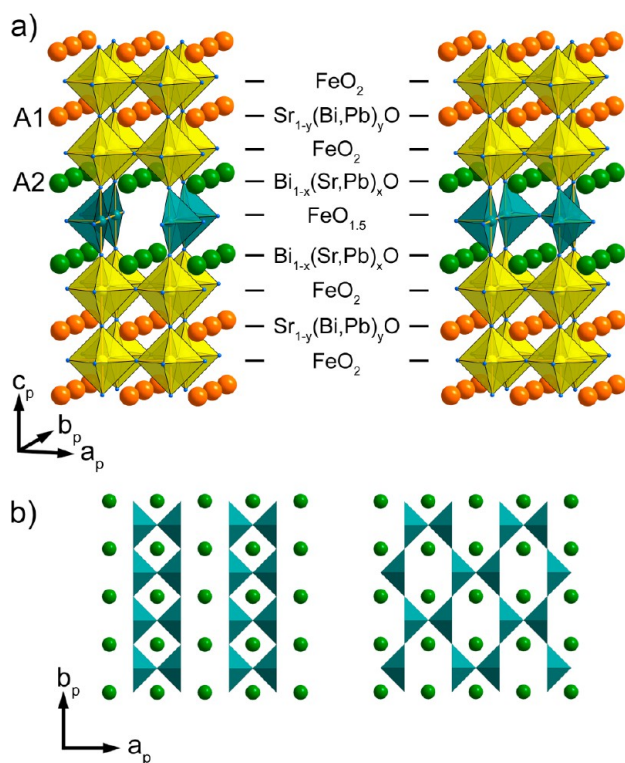


Figure 13. (a) Two idealized models of the inclusion structure: chain or chess-board ordering of oxygen vacancies. (b) Top view of the two types of FeO_{1.5} layers.

Bi₃(Sr,Pb)Fe₄O_{11.5}; they differ just by two $\text{--Sr}_{1-y}(\text{Bi,Pb})_y\text{O--FeO}_2\text{--}$ layers.

Although the $(\text{Bi}_{1-z}\text{Sr}_z)\text{FeO}_{3-y}$ system has been intensely studied, materials with the described structure and composition have not been reported before. Mössbauer spectroscopy confirms that in the $(\text{Bi}_{1-z}\text{Sr}_z)\text{FeO}_{3-y}$ system (at least for $z \leq 0.67$) Fe has the oxidation state +3 and the anion deficiency is accommodated through the formation of oxygen vacancies.^{62–66} However, still the exact arrangement of the vacancies is not completely clear. According to different Mössbauer studies, in addition to octahedral coordination, Fe has tetrahedral^{62,66} or both tetrahedral and pyramidal coordination.^{63,64} TEM studies demonstrate the complex microstructure of $(\text{Bi}_{1-z}\text{Sr}_z)\text{FeO}_{3-y}$ crystals ($0.2 \leq z \leq 0.67$,^{67,68} $z = 0.67$,⁶³ $z = 0.25$ ⁶⁹). Splitting the structure into relatively extended oxygen-complete and oxygen-deficient blocks was proposed for the $0.2 \leq z \leq 0.67$ region,⁵⁹ with a tetragonal-pyramidal coordination of Fe³⁺ in the oxygen-deficient block. For the $z = 2/3$ compound, an intralayer ordering of the Sr and Bi cations was also observed.⁶³ For $z = 0.85$ material, an ordering of oxygen vacancies, similar to that in $\text{Sr}_8\text{Fe}_8\text{O}_{23}$, was suggested.⁷⁰ Apparently, none of these situations is realized in the locally observed $\text{Bi}_2(\text{Sr,Pb})\text{Fe}_3\text{O}_{8.5}$ and $\text{Bi}_3(\text{Sr,Pb})\text{Fe}_4\text{O}_{11.5}$ structures in our samples. Here, the layered ordering of the oxygen vacancies and the interlayer ordering of the A cations are coupled. From simple electrostatic considerations, one could expect segregation of the Sr^{2+} cations near the oxygen-deficient electrically neutral FeO_{1.5} layers, rather than next to negatively charged FeO₂ layers, which would be more attractive for the Bi³⁺ cations. However, the experimentally observed structure is just the opposite. A plausible explanation for the segregation of the Bi³⁺ cations near vacant oxygen positions has been provided

by Withers et al.,⁶⁷ who pointed out that the stereochemical activity of the lone pair on the Bi³⁺ cation could play a role, acquiring sufficient free space if directed toward a vacant oxygen position. The fact that the $\text{Bi}_2(\text{Sr,Pb})\text{Fe}_3\text{O}_{8.5}$ and $\text{Bi}_3(\text{Sr,Pb})\text{Fe}_4\text{O}_{11.5}$ structures have never been observed before might be related to their stabilization by the epitaxial strain created by the CS matrix.

Concerning the “hairpin”-like defects, one should recall the nonstoichiometric oxides derived from the ReO₃ or rutile TiO₂ structures.^{71–73} Because of the absence of the A cations in the octahedral framework, the CS mechanism affects only the connectivity scheme of the octahedra and does not change the coordination number of the metal. TEM data confirm that it is very common for nonstoichiometric oxides that CS planes with different orientations coexist within one crystal. The “hairpin”-like defects have also been observed both in TiO_{2-δ}¹⁰ and $\text{W}_n\text{O}_{3n-2}$.⁷⁴ Van Landuyt and Amelinckx¹⁰ proposed that in TiO_{2-δ} “hairpins” are involved in the generation mechanism of the CS structures. For the other CS phases, however, other mechanisms were developed: for example, one based on cooperative cation migration⁷⁵ or one implying a dislocation-limited anion vacancy loop.⁷⁶ Therefore, it is more likely that the formation of CS planes in oxygen-deficient oxides occurs by various mechanisms, depending on the composition of the compound. The CS generation in the perovskite-based materials is still an open question. For example, in the Pb–Fe–O system the CS plane formation goes through an intermediate intergrowth structure with alternating perovskite and Aurivillius-type blocks.⁷⁷ However, in other systems none of the microstructural features, which could be related to the presence of an intermediate phase, were observed. Concerning the Pb–Sr–Bi–Fe–O system studied here, it is difficult (although not impossible) to claim that “hairpins” in $\text{Pb}_2\text{Sr}_2\text{Bi}_2\text{Fe}_6\text{O}_{16}$ are involved in the CS growth. Apparently, this type of defect is characteristic for Sr-based CS plane structures due to the specific geometric conditions discussed above and does not appear in the Ba-based or Pb/Bi-based systems. Thus, CS plane growth through the “hairpin” defects cannot be a universal mechanism for CS plane formation in perovskites.

■ ASSOCIATED CONTENT

Supporting Information

Text, figures, and tables giving experimental and simulated X-ray powder diffraction patterns of $\text{Pb}_2\text{Sr}_2\text{Bi}_2\text{Fe}_6\text{O}_{16}$, additional HAADF- and ABF-STEM images and electron diffraction patterns from the different areas of the $\text{Pb}_2\text{Sr}_2\text{Bi}_2\text{Fe}_6\text{O}_{16}$ crystals, an EELS map, and atomic coordinates for the $\text{Bi}_3(\text{Sr,Pb})\text{Fe}_4\text{O}_{11.5}$ structure model. This material is available free of charge via the Internet at <http://pubs.acs.org>.

■ AUTHOR INFORMATION

Corresponding Author

*M.B.: e-mail, Maria.Batuk@uantwerpen.be; tel, 00 32 32653695.

Author Contributions

The manuscript was written through contributions of all authors. All authors have given approval to the final version of the manuscript.

Notes

The authors declare no competing financial interest.

ACKNOWLEDGMENTS

M.B., D.B., and J.H. acknowledge funding from the Research Foundation—Flanders under grant number G018409N. M.B. is grateful to Emrah Yücelen from the FEI (Eindhoven, The Netherlands) for his help in performing atomic resolution STEM-EDX measurements. S.T. acknowledges the fund for scientific research Flanders (FWO) for financial support (G004613N and G004413N). G.V.T. acknowledges the European Research Council, ERC grant no. 246791—COUNTATOMS.

REFERENCES

- (1) Anderson, J. S. *J. Phys. Colloq.* **1977**, *38*, 17–27.
- (2) Ruiz-Morales, J. C.; Canales-Vázquez, J.; Savaniu, C.; Marrero-López, D.; Zhou, W.; Irvine, J. T. S. *Nature* **2006**, *439*, 568–571.
- (3) Specht, E. D.; Goyal, A.; Li, J.; Martin, P. M.; Li, X.; Rupich, M. *W. Appl. Phys. Lett.* **2006**, *89*, 162510.
- (4) Van Tendeloo, G.; Lebedev, O. I.; Hervieu, M.; Raveau, B. *Rep. Prog. Phys.* **2004**, *67*, 1315–1365.
- (5) Van Landuyt, J.; De Ridder, R.; Gevers, R.; Amelinckx, S. *Mater. Res. Bull.* **1970**, *5*, 353–362.
- (6) Magnéli, A. *Acta Crystallogr.* **1953**, *6*, 495–500.
- (7) Magnéli, A.; Blomberg-Hansson, B.; Kihlberg, L.; Sundkvist, G. *Acta Chem. Scand.* **1955**, *9*, 1382–1390.
- (8) Gadó, P.; Holmberg, B.; Magnéli, A.; Kallner, A. *Acta Chem. Scand.* **1965**, *19*, 2010–2011.
- (9) Bursill, L. A.; Hyde, B. G. *J. Solid State Chem.* **1972**, *4*, 430–446.
- (10) Van Landuyt, J.; Amelinckx, S. *J. Solid State Chem.* **1973**, *6*, 222–229.
- (11) England, P. J.; Booth, J.; Tilley, R. J. D.; Ekström, T. *J. Solid State Chem.* **1982**, *44*, 60–74.
- (12) Anderson, M. T.; Vaughney, J. T.; Poeppelmeier, K. R. *Chem. Mater.* **1993**, *5*, 151–165.
- (13) Hodges, J. P.; Short, S.; Jorgensen, J. D.; Xiong, X.; Dabrowski, B.; Mini, S. M.; Kimball, C. W. *J. Solid State Chem.* **2000**, *151*, 190–209.
- (14) D'Hondt, H.; Abakumov, A. M.; Hadermann, J.; Kalyuzhnaya, A. S.; Rozova, M. G.; Antipov, E. V.; Van Tendeloo, G. *Chem. Mater.* **2008**, *20*, 7188–7194.
- (15) Tsujimoto, Y.; Tassel, C.; Hayashi, N.; Watanabe, T.; Kageyama, H.; Yoshimura, K.; Takano, M.; Ceretti, M.; Ritter, C.; Paulus, W. *Nature* **2007**, *450*, 1062–1065.
- (16) Caignaert, V.; Nguyen, N.; Hervieu, M.; Raveau, B. *Mater. Res. Bull.* **1985**, *20*, 479–484.
- (17) Alonso, J. A.; Martínez-Lope, M. J.; García-Muñoz, J. L.; Fernández-Díaz, M. T. *J. Phys.: Condens. Matter* **1997**, *9*, 6417–6426.
- (18) Er-Rakho, L.; Michel, C.; Raveau, B. *J. Solid State Chem.* **1988**, *73*, 514–519.
- (19) Hadermann, J.; Van Tendeloo, G.; Abakumov, A. M. *Acta Crystallogr., Sect. A* **2005**, *61*, 77–92.
- (20) Bougerol, C.; Gorius, M. F.; Grey, I. E. *J. Solid State Chem.* **2002**, *169*, 131–138.
- (21) Abakumov, A. M.; Hadermann, J.; Bals, S.; Nikolaev, I. V.; Antipov, E. V.; Van Tendeloo, G. *Angew. Chem., Int. Ed.* **2006**, *45*, 6697–6700.
- (22) Abakumov, A. M.; Hadermann, J.; Van Tendeloo, G.; Antipov, E. V. *J. Am. Ceram. Soc.* **2008**, *91*, 1807–1813.
- (23) Abakumov, A. M.; Hadermann, J.; Batuk, M.; D'Hondt, H.; Tyablikov, O. A.; Rozova, M. G.; Pokholok, K. V.; Filimonov, D. S.; Sheptyakov, D. V.; Tsirlin, A. A.; Niernann, D.; Hemberger, J.; Van Tendeloo, G.; Antipov, E. V. *Inorg. Chem.* **2010**, *49*, 9508–9516.
- (24) Raynova-Schwarten, V.; Massa, W.; Babel, D. Z. *Anorg. Allg. Chem.* **1997**, *623*, 1048–1054.
- (25) Tzvetkov, P.; Petrova, N.; Kovacheva, D. *J. Alloys Compd.* **2009**, *485*, 862–866.
- (26) Nikolaev, I. V.; D'Hondt, H.; Abakumov, A. M.; Hadermann, J.; Balagurov, A. M.; Bobrikov, I. A.; Sheptyakov, D. V.; Pomjakushin, V. Y.; Pokholok, K. V.; Filimonov, D. S.; Van Tendeloo, G.; Antipov, E. V. *Phys. Rev. B* **2008**, *78*, 024426.
- (27) Hadermann, J.; Abakumov, A. M.; Perkisas, T.; D'Hondt, H.; Tan, H.; Verbeeck, J.; Filonenko, V. P.; Antipov, E. V.; Van Tendeloo, G. *J. Solid State Chem.* **2010**, *183*, 2190–2195.
- (28) Tzvetkov, P.; Kovacheva, D.; Nihtianova, D.; Ruskov, T. *Bulg. Chem. Commun.* **2011**, *43*, 339–345.
- (29) Korneychik, O. E.; Batuk, M.; Abakumov, A. M.; Hadermann, J.; Rozova, M. G.; Sheptyakov, D. V.; Pokholok, K. V.; Filimonov, D. S.; Antipov, E. V. *J. Solid State Chem.* **2011**, *184*, 3150–3157.
- (30) Tzvetkov, P.; Kovacheva, D.; Nihtianova, D.; Velichkova, N.; Ruskov, T. *Bulg. Chem. Commun.* **2012**, *44*, 137–145.
- (31) Abakumov, A. M.; Batuk, M.; Tsirlin, A. A.; Tyablikov, O. A.; Sheptyakov, D. V.; Filimonov, D. S.; Pokholok, K. V.; Zhidal, V. S.; Rozova, M. G.; Antipov, E. V.; Hadermann, J.; Van Tendeloo, G. *Inorg. Chem.* **2013**, *52*, 7834–7843.
- (32) Batuk, M.; Tyablikov, O. A.; Tsirlin, A. A.; Kazakov, S. M.; Rozova, M. G.; Pokholok, K. V.; Filimonov, D. S.; Antipov, E. V.; Abakumov, A. M.; Hadermann, J. *Mater. Res. Bull.* **2013**, *48*, 3459–3465.
- (33) Barrier, N.; Lebedev, O. I.; Seikh, M. M.; Porcher, F.; Raveau, B. *Inorg. Chem.* **2013**, *52*, 6073–6082.
- (34) Hadermann, J.; Abakumov, A. M.; Nikolaev, I. V.; Antipov, E. V.; Van Tendeloo, G. *Solid State Sci.* **2008**, *10*, 382–389.
- (35) Abakumov, A. M.; Batuk, D.; Hadermann, J.; Rozova, M. G.; Sheptyakov, D. V.; Tsirlin, A. A.; Niernann, D.; Waschkowski, F.; Hemberger, J.; Van Tendeloo, G.; Antipov, E. V. *Chem. Mater.* **2011**, *23*, 255–265.
- (36) Batuk, D.; Batuk, M.; Abakumov, A. M.; Tsirlin, A. A.; McCammon, C.; Dubrovinsky, L.; Hadermann, J. *Inorg. Chem.* **2013**, *52*, 10009–10020.
- (37) Lepoittevin, C.; Hadermann, J.; Malo, S.; Pérez, O.; Van Tendeloo, G.; Hervieu, M. *Inorg. Chem.* **2009**, *48*, 8257–8262.
- (38) Malo, S.; Lepoittevin, C.; Pérez, O.; Hébert, S.; Van Tendeloo, G.; Hervieu, M. *Chem. Mater.* **2010**, *22*, 1788–1797.
- (39) Nellist, P. D.; Pennycook, S. J. *Ultramicroscopy* **1999**, *78*, 111–124.
- (40) Findlay, S. D.; Shibata, N.; Sawada, H.; Okunishi, E.; Kondo, Y.; Yamamoto, T.; Ikuhara, Y. *Appl. Phys. Lett.* **2009**, *95*, 191913.
- (41) Bosman, M.; Keast, V.; García-Muñoz, J.; D'Alfonso, A.; Findlay, S.; Allen, L. J. *Phys. Rev. Lett.* **2007**, *99*, 1–4.
- (42) Kimoto, K.; Asaka, T.; Nagai, T.; Saito, M.; Matsui, Y.; Ishizuka, K. *Nature* **2007**, *450*, 702–704.
- (43) D'Alfonso, A. J.; Freitag, B.; Klenov, D.; Allen, L. J. *Phys. Rev. B* **2010**, *81*, 2–5.
- (44) Chu, M.-W.; Liou, S. C.; Chang, C.-P.; Choa, F.-S.; Chen, C. H. *Phys. Rev. Lett.* **2010**, *104*, 1–4.
- (45) Muller, D. A. *Nat. Mater.* **2009**, *8*, 263–270.
- (46) Rossell, M. D.; Abakumov, A. M.; Ramasse, Q. M.; Erni, R. *ACS Nano* **2013**, *7*, 3078–3085.
- (47) Tan, H.; Turner, S.; Yücelen, E.; Verbeeck, J.; Van Tendeloo, G. *Phys. Rev. Lett.* **2011**, *107*, 107602.
- (48) Turner, S.; Lazar, S.; Freitag, B.; Egoavil, R.; Verbeeck, J.; Put, S.; Strauven, Y.; Van Tendeloo, G. *Nanoscale* **2011**, *3*, 3385–3390.
- (49) Turner, S.; Verbeeck, J.; Ramezanipour, F.; Greedan, J. E.; Van Tendeloo, G.; Botton, G. A. *Chem. Mater.* **2012**, *24*, 1904–1909.
- (50) Turner, S.; Egoavil, R.; Batuk, M.; Abakumov, A. M.; Hadermann, J.; Verbeeck, J.; Van Tendeloo, G. *Appl. Phys. Lett.* **2012**, *101*, 241910.
- (51) Koch, C. *Determination of core structure periodicity and point defect density along dislocations*; Arizona State University, 2002.
- (52) Van Smaalen, S. *Incommensurate Crystallography*; Oxford University Press: Oxford, U.K., 2007.
- (53) Van der Laan, G.; Kirkman, I. W. *J. Phys.: Condens. Matter* **1992**, *4*, 4189–4204.
- (54) Van Aken, P. A.; Liebscher, B. *Phys. Chem. Miner.* **2002**, *29*, 188–200.
- (55) Tatsumi, K.; Muto, S.; Nishida, I.; Ruzs, J. *Appl. Phys. Lett.* **2010**, *96*, 201911.

- (56) Rossell, M. D.; Abakumov, A. M.; Van Tendeloo, G.; Pardo, J. A.; Santiso, J. *Chem. Mater.* **2004**, *16*, 2578–2584.
- (57) Rossell, M. D.; Abakumov, A. M.; Van Tendeloo, G.; Lomakov, M. V.; Istomin, S. Y.; Antipov, E. V. *Chem. Mater.* **2005**, *17*, 4717–4726.
- (58) Pérez, O.; Mellenne, B.; Retoux, R.; Raveau, B.; Hervieu, M. *Solid State Sci.* **2006**, *8*, 431–443.
- (59) Yoshiasa, A.; Takeno, S.; Iishi, K. *Mineral. J.* **1992**, *16*, 40–48.
- (60) Abakumov, A. M.; Rossell, M. D.; Gutnikova, O. Y.; Drozhzhin, O. A.; Leonova, L. S.; Dobrovolsky, Y. A.; Istomin, S. Y.; Van Tendeloo, G.; Antipov, E. V. *Chem. Mater.* **2008**, *20*, 4457–4467.
- (61) Wojdyr, M. *J. Appl. Crystallogr.* **2010**, *43*, 1126–1128.
- (62) Li, J.; Duan, Y.; He, H.; Song, D. *J. Alloys Compd.* **2001**, *315*, 259–264.
- (63) Lepoittevin, C.; Malo, S.; Barrier, N.; Nguyen, N.; Van Tendeloo, G.; Hervieu, M. *J. Solid State Chem.* **2008**, *181*, 2601–2609.
- (64) Pokatilov, V. V.; Pokatilov, V. S.; Sigov, A. S.; Cherepanov, V. M. *Inorg. Mater.* **2009**, *45*, 683–688.
- (65) Troyanchuk, I. O.; Bushinsky, M. V.; Karpinsky, D. V.; Sirenko, V.; Sikolenko, V.; Efimov, V. *Eur. Phys. J. B* **2010**, *73*, 375–381.
- (66) Folcke, E.; Le Breton, J. M.; Bréard, Y.; Maignan, A. *Solid State Sci.* **2010**, *12*, 1387–1392.
- (67) Withers, R. L.; Bourgeois, L.; Balamurugan, K.; Harish Kumar, N.; Santhosh, P. N.; Wu, L. *J. Solid State Chem.* **2009**, *182*, 2176–2184.
- (68) Withers, R. L.; Schiemer, J.; Bourgeois, L.; Norén, L.; Liu, Y. *J. Phys. Conf. Ser.* **2010**, *226*, 012015.
- (69) Pachoud, E.; Bréard, Y.; Martin, C.; Maignan, A.; Abakumov, A. M.; Suard, E.; Smith, R. I.; Suchomel, M. R. *Solid State Commun.* **2012**, *152*, 331–336.
- (70) Eriksson, A. K.; Lindberg, F.; Svensson, G.; Svedlindh, P.; Henry, P. F.; Eriksson, S.-G.; Knee, C. S. *J. Solid State Chem.* **2008**, *181*, 2031–2040.
- (71) Magnéli, A.; Hofman-Bang, N.; Gjertsen, P. *Acta Chem. Scand.* **1948**, *2*, 501–517.
- (72) Wadsley, A. D. *Rev. Pure Appl. Chem.* **1955**, *5*, 165–193.
- (73) Kihlberg, L. *Ark. Kemi* **1963**, *21*, 443–460.
- (74) Roberts, M. W.; Thomas, J. M.; Anderson, J. S.; Tilley, R. J. D. *Surf. Defect Prop. Solids* **1974**, 1–56.
- (75) Andersson, S.; Wadsley, A. D. *Nature* **1966**, *211*, 581–583.
- (76) Anderson, J. S.; Hyde, B. G. *Bull. Soc. Chim. Fr.* **1965**, 1215.
- (77) Batuk, D.; Hadermann, J.; Abakumov, A. M.; Vranken, T.; Hardy, A.; Van Bael, M.; Van Tendeloo, G. *Inorg. Chem.* **2011**, *50*, 4978–4986.
- (78) Although in previous papers the orientation of CS planes in $A_nB_nO_{3n-2}$ was defined as $(\bar{1}01)_p$, in this contribution it will be considered as $(101)_p$ for consistency with other $1/2[110]_p(h0l)_p$ CS structures. These options are interchangeable.